

Wave energy cascade in forced-dissipative one-layer shallow-water flows

Pierre Augier^{1,2†}, and Erik Lindborg¹

¹Linné Flow Centre, KTH Mechanics, SE-100 44 Stockholm, Sweden

²Department of Applied Mathematics and Theoretical Physics, University of Cambridge, Cambridge CB3 0WA, United Kingdom

(Received ?; revised ?; accepted ?. - To be entered by editorial office)

The dynamics of one-layer shallow-water flows forced in medium-scale wave modes and dissipation acting at small scales is investigated by means of theoretical analysis and numerical simulations with resolutions up to 7680². We first focus on the non-rotating case for which a statistically stationary regime is obtained for all resolutions and Froude numbers $F_f = \varepsilon/(k_f c)$, where ε is the energy dissipation rate, k_f the forcing wave number and c the wave speed. All the injected energy goes into a downscale energy cascade. Consequently, the spectral energy flux is constant and positive between the forcing wave number and the wave numbers where dissipation is active. The spectral energy flux is exactly equipartitioned between kinetic and potential energy. An exact third order structure function law of Kolmogorov type is derived and numerically verified. However, the downscale cascade is less efficient than in three-dimensional Navier-Stokes turbulence, since the mean energy of the statistically stationary flow scales as $\sqrt{\varepsilon c/k_f}$ and varies with the dissipative scale. Moreover, the spectra scale as k^{-2} and the structure functions of order larger than two scale approximately as r . This intermittent scaling is explained by a simple model based on the assumption that the statistics is totally determined by shocks. It is verified that the dynamics is not drastically modified by system rotation as long as the forcing wave number is larger than the deformation wave number $k_d = f/c$, where f is the Coriolis parameter.

1. Introduction

The shallow-water models have been widely used to study basic mechanisms occurring in geophysical flows (see for example Vallis 2006). These models are based on the hydrostatic approximation which is extremely well satisfied for a very wide range of scales in the oceans and in the atmosphere and on which are based the so-called primitive equations. They also rely on a stronger hypothesis regarding the density stratification. The fluid is assumed to be structured in a limited number of thin homogeneous layers, which leads to equations involving only two-dimensional operators. However, as long as there is no overturning, the shallow-water model in the limit of a large number of layers and the primitive equations describe the same dynamics. In the opposite limit, two models are particularly important from the theoretical point of view. The two-layer shallow-water model captures the baroclinic instability which is of primary importance for the dynamics of the oceans and of the atmosphere (Vallis 2006; Wirth 2013). The equations of the one-layer shallow-water model are very similar to the two-dimensional compressible Navier-Stokes equations. The one-layer model does not capture the baroclinic instability but it is one of the simplest hydrodynamic models with coexisting eigenmodes of the

† Email address for correspondence: p.augier@damtp.cam.ac.uk

linearized operator with zero linear frequency and with finite non-zero linear frequency, $\omega = \pm\omega_l = \pm\sqrt{f^2 + c^2k^2}$, where f is the Coriolis parameter, c the wave speed and $k = |\mathbf{k}|$ the wave number.

For geophysical applications, it is convenient to consider the limits for which the linear frequency ω_l is much larger than the characteristic nonlinear frequency $\omega_{nl} = U k$, where U is a characteristic velocity. In the limit $f/\omega_{nl} \sim ck/\omega_{nl} \rightarrow \infty$, one can obtain a quasi-geostrophic one-layer shallow-water model, i.e. derive self-consistent evolution equations for the 0-linear-frequency variable, the Charney potential vorticity. In this limit, the dynamics of the 0-linear-frequency variable is totally decorrelated from the fast waves. For finite rotation and wave speed, there are slow balanced motions, which are associated with relatively weak non-zero linear frequency modes. When $\omega_{nl}(k) \ll \omega_l(k)$, there is only a weak interaction between waves and the balanced modes. Due to its relative simplicity, the one-layer shallow-water model has been used to study issues like the projection on the balanced manifold (Lorenz 1980; Mohebalhojeh & Dritschel 2000) and the production of waves by balanced flows (Farge & Sadourny 1989; Lahaye & Zeitlin 2012; Vanneste 2013). **In this study, we consider the same model in order to address a related but different issue.**

Balanced flows have a dynamics which is very similar to two-dimensional turbulence. In the quasi-geostrophic limit, the space-averaged energy and the space-averaged potential enstrophy are conserved, positive definite and proportional in Fourier space. This leads, **as in two-dimensional turbulence**, to an upscale energy cascade and a downscale enstrophy cascade. Thus, the small-scale dissipation vanishes in the limit of zero viscosity. In contrast to this, statistical mechanics indicates that wave energy should be transferred towards small scales (Warn 1986). Numerical simulations have shown that long waves lose their energy by transferring it to shorter waves (Sadourny 1975; Farge & Sadourny 1989; Yuan & Hamilton 1994). The mechanism of a wave cascade has been proposed to explain the attraction towards the balanced flows (Sadourny 1975). Yuan & Hamilton (1994) showed that statistically stationary shallow-water flows can be obtained forcing quasi-geostrophic modes at large scales and with dissipation only at small scales. **They propose that the $k^{-5/3}$ spectra that are observed at the atmospheric meso-scales** (Nastrom & Gage 1985; Frehlich & Sharman 2010) **and reproduced by some atmospheric models based on the primitive equations** (Koshyk & Hamilton 2001; Skamarock 2004; Hamilton *et al.* 2008) **could be reproduced by the one-layer shallow-water model by a downscale energy cascade of waves.**

However, few studies have investigated the dynamics of the downscale energy cascade of waves in shallow-water models. Most numerical studies have investigated decaying flows and have not focused on the cascade (Farge & Sadourny 1989; Larichev & McWilliams 1991; Spall & McWilliams 1992; Polvani *et al.* 1994; Lahaye & Zeitlin 2012). Moreover, there are strong discrepancies between different numerical results and between these results and available theoretical results. Farge & Sadourny (1989) reported spectra scaling like k^{-4} whereas those shown by Lahaye & Zeitlin (2012) scale like k^{-6} .

Some predictions are based on the weak wave turbulence formalism (Zakharov *et al.* 1992; Nazarenko 2011). In the case of inertial-gravity waves, Falkovich & Medvedev (1992) showed that the exact solutions of the kinetic equation corresponding to a constant downscale energy flux is associated with a spectrum scaling like $E(k) \sim P^{2/3}k^{-8/3}$. However, as pointed out by Falkovich & Meyer (1996) when the dispersion is small enough, waves moving in the same direction have the same velocity and interact strongly, which can lead to the formation of shocks. **In this case, the weak wave turbulence formalism is unable to give valuable results.** Such sharp and long structures have been observed in many simulations (Farge & Sadourny 1989; Polvani *et al.* 1994; Lahaye & Zeitlin 2012) but **their effects** are not well understood. Kuznetsov (2004) predicted that a flow domi-

nated by shocks should be associated with spectra scaling like $E(k) \sim k^{-2}$. Falkovich & Meyer (1996) simulated acoustic turbulence dominated by shocks and reported spectra in agreement with this theoretical prediction. The shocks also lead to very strong intermittency, as demonstrated by Bouchaud *et al.* (1995) and Weinan *et al.* (1997) in the case of Burgers turbulence.

The dynamics of waves in complex shallow-water flows is not well understood. Our long-term goal is to understand this dynamics which involves interactions between balance and unbalance parts of the flow. However, even the wave cascade without balance flow is not well understood. A statistically stationary wave cascade has never been simulated at high resolution. Is it possible to obtain a statistically stationary state in the very fast wave regime, and how does the mean energy in this hypothetical regime depends on the forcing and the wave speed? How does the energy spectra scale as a function of the input parameters? All these questions are open and straightforward simulations may provide the answers.

Yuan & Hamilton (1994) and Falkovich & Meyer (1996) carried out forced dissipated simulation of the one-layer shallow water model and acoustic turbulence, respectively. However, the resolution in both studies was quite coarse (386² and 101² grid points, respectively) so that the inertial range was very narrow. Moreover, Falkovich & Meyer (1996) used a very particular type of strongly anisotropic forcing with waves in only one direction while Yuan & Hamilton (1994) forced in geostrophic modes which severely complicates the interpretation.

In this paper, we investigate the dynamics of one-layer shallow-water flows forced in the wave modes by means of high resolution numerical simulations with up the 7680² grid points. The model is described in section 2. We then derive some new theoretical results for this model and for turbulence dominated by shocks (section 3). The numerical methods and the forcing are described in section 4. The main numerical results corresponding to the simple case without global rotation are presented in section 5. We investigate the sensibility of the non-rotating results to a moderate rotation (section 6).

2. The one-layer shallow-water model

2.1. Physical system and governing equations

We consider a thin layer of fluid over a flat bottom and with a free surface. Under the assumption that the characteristic horizontal scale of the flow L is much larger than the mean layer thickness H_0 , it can be shown that the pressure is only a function of the local layer thickness $H(x, y)$, i.e. that the flow is hydrostatic. Further assuming that the horizontal flow is vertically invariant, it can be shown that the shallow-water system is governed by the Saint-Venant equations (see for example Vallis 2006)

$$(\partial_t + \mathbf{u} \cdot \nabla) \mathbf{u} = -c^2 \nabla h - f \mathbf{e}_z \wedge \mathbf{u} + \nu \nabla^2 \mathbf{u}, \quad (2.1)$$

$$\partial_t h = -\nabla \cdot (h \mathbf{u}). \quad (2.2)$$

where \mathbf{u} is the horizontal velocity, $h = H/H_0$ the normalized layer thickness, ∇ the horizontal gradient, ν the kinetic viscosity, f the Coriolis parameter and $c = \sqrt{gH_0}$, with g the gravitational acceleration. In the following, the Coriolis parameter is assumed to be spatially homogeneous.

2.2. Eigenmodes of the linearized equations

Neglecting the non-linear and the dissipative terms, the governing equations can be rewritten as

$$\partial_t q = 0, \quad \partial_t d = a \quad \text{and} \quad \partial_t a = -c^2 \varkappa^2 d, \quad (2.3)$$

where $q = \zeta - f\eta$ is the linear Charney potential vorticity, $d = \nabla \cdot \mathbf{u}$ the horizontal divergence, $a = -c^2 \nabla^2 \eta + f\zeta$ an ageostrophic variable and $\varkappa^2 = k_d^2 - \nabla^2$ the Helmholtz operator, with $k_d = f/c$ the deformation wave number. Here, $\eta = h - 1$ is the normalized surface displacement and $\zeta = \mathbf{e}_z \cdot (\nabla \wedge \mathbf{u})$ is the vertical component of the vorticity. The dispersion relation is $\omega^2 = \omega_l^2$, where

$$\omega_l(\mathbf{k}) \equiv c \sqrt{k_d^2 + |\mathbf{k}|^2} = \sqrt{f^2 + c^2 |\mathbf{k}|^2}, \quad (2.4)$$

which implies that in the non-rotating case the waves are non-dispersive. The eigenfunctions of the linear operator are the prograde and retrograde linear waves with positive and negative frequencies, respectively. Denoting the prograde quantities by the index $+$, the retrograde quantities by the index $-$ and the temporal and spatial Fourier transform by a tilde, we have by definition $a = a_+ + a_-$, $d = d_+ + d_-$, $\tilde{\partial}_t a_{\pm} = \mp i \omega_l \tilde{a}_{\pm}$ and $\tilde{\partial}_t d_{\pm} = \mp i \omega_l \tilde{d}_{\pm}$. The linearized governing equations for the waves can be rewritten as $i \tilde{a}_{\pm} = \pm \omega_l \tilde{d}_{\pm}$, which gives $\tilde{a}_{\pm} = \tilde{a}/2 \pm \omega_l d/(2i)$.

2.3. Conserved quantities

The non-dissipative one-layer shallow-water equations conserve a local quantity along the trajectories of the fluid particles, the Ertel potential vorticity $\mathcal{Q} = \zeta_a/h$, where $\zeta_a = \zeta + f$ is the absolute vorticity. Note that since the lagrangian derivative of the Ertel potential vorticity is $D_t \mathcal{Q} = 0$, the space-averaged Ertel potential vorticity is not conserved $\partial_t \langle \mathcal{Q} \rangle_{\mathbf{x}} = \langle d \mathcal{Q} \rangle_{\mathbf{x}} \neq 0$, where the brackets $\langle \rangle_{\mathbf{x}}$ denote the space average. In the case of two-dimensional turbulence, it can be shown that the energy can not cascade towards small scales due to the constraints that the enstrophy $\langle \zeta^2/2 \rangle_{\mathbf{x}}$ is conserved and that the spectra of energy and enstrophy are proportional (Kraichnan 1967). This result was further extended by Charney (1971) to the case of quasi-geostrophic turbulence using the analogy between the enstrophy and the Charney linear potential enstrophy $\langle q^2/2 \rangle_{\mathbf{x}}$, where q is the linear potential vorticity equal in the shallow water case to $q = \zeta - f\eta$. Note, however, that the analogy does not hold for the nonlinear Ertel potential vorticity \mathcal{Q} and that the local conservation of \mathcal{Q} is a much weaker constraint for the dynamics of the flows.

The non-dissipative one-layer shallow-water equations also conserve some space-averaged quantities. For example, since

$$(D_t + d)\zeta_a = 0 \Rightarrow \partial_t \langle \zeta_a \rangle_{\mathbf{x}} = 0, \quad (2.5)$$

the space-averaged absolute vorticity $\langle \zeta_a \rangle_{\mathbf{x}}$ is conserved. Since the governing equation for the thickness h and the mass flux $\mathbf{J} = h\mathbf{u}$ are

$$(D_t + d)h = 0, \quad (2.6)$$

$$(D_t + d)\mathbf{J} = -\nabla E_P - f\mathbf{e}_z \wedge \mathbf{J}, \quad (2.7)$$

where $E_P = c^2 h^2/2$ is the total potential energy, the space-averaged thickness $\langle h \rangle_{\mathbf{x}}$ is conserved and the kinetic momentum $\langle \mathbf{J} \rangle_{\mathbf{x}}$ is conserved in the absolute not-rotating reference frame. Note that in contrast to the case of the Navier-Stokes equations, the dissipative shallow-water equations do not conserve $\langle \mathbf{J} \rangle_{\mathbf{x}}$, even with a Newtonian viscous operator.

The non-dissipative one-layer shallow-water equations also conserve the space-averaged total energy, the local energy being the sum of the local potential energy (PE), $E_P = c^2 h^2/2$, and the local kinetic energy (KE), $E_K = \mathbf{J} \cdot \mathbf{u}/2$. Using (2.1), (2.6) and (2.7), it is straightforward to show that

$$(D_t + d)E_K = -\mathbf{u} \cdot \nabla E_P, \quad (2.8)$$

$$(D_t + d)E_P = -E_P \nabla \cdot \mathbf{u}. \quad (2.9)$$

The space-averaged conversion from potential energy to kinetic energy is equal to $C = -\langle \mathbf{u} \cdot \nabla E_P \rangle_{\mathbf{x}} = \langle E_P \nabla \cdot \mathbf{u} \rangle_{\mathbf{x}}$. The total potential energy can be split in three parts

$$E_P = c^2/2 + c^2\eta + c^2\eta^2/2. \quad (2.10)$$

The first term corresponds the potential energy of the state with null surface displacement. The second term is a contribution to the potential energy which is zero in average. We call the third term $E_A = c^2\eta^2/2$ the available potential energy (APE). Its space-average is indeed equal to the space-averaged APE.

3. Theoretical analysis

3.1. Analysis of the wave energy cascade

3.1.1. Formulation of the spectral energy budget for non-quadratic energy

In order to analyze the flux of energy, we derive the spectral energy budget, i.e. the governing equations for spectral KE and APE functions. This is not as straightforward as in incompressible turbulence since the expression of the kinetic energy $E_K = \mathbf{J} \cdot \mathbf{u}/2$ is not quadratic. In order to define the spectral KE function, we use the relation

$$\langle E_K \rangle_{\mathbf{x}} = \sum_{\mathbf{k}} (\mathbf{u}, \mathbf{J})_{\mathbf{k}}/2, \quad (3.1)$$

where

$$(\mathbf{a}, \mathbf{b})_{\mathbf{k}} \equiv \Re\{\hat{\mathbf{a}}(\mathbf{k})^* \cdot \hat{\mathbf{b}}(\mathbf{k})\}, \quad (3.2)$$

where \Re denotes the real part, \mathbf{k} is the wave number and the hat denotes the Fourier transform. The spectral KE function can therefore be defined as

$$E_K(\mathbf{k}) \equiv (\mathbf{u}, \mathbf{J})_{\mathbf{k}}/2, \quad (3.3)$$

such as $\langle E_K \rangle_{\mathbf{x}} = \sum_{\mathbf{k}} E_K(\mathbf{k})$. Similarly, the PE can be written as the sum over all wave numbers of the spectral PE function $E_P(\mathbf{k}) = c^2|\hat{h}|^2/2 = c^2(h, h)_{\mathbf{k}}/2$, where, by definition,

$$(a, b)_{\mathbf{k}} \equiv \Re\{\hat{a}(\mathbf{k})^* \hat{b}(\mathbf{k})\}. \quad (3.4)$$

The equation for the spectral KE and PE functions can be written as

$$\partial_t E_K(\mathbf{k}) = T_K(\mathbf{k}) + C_K(\mathbf{k}), \quad (3.5)$$

$$\partial_t E_P(\mathbf{k}) = T_P(\mathbf{k}) - C_P(\mathbf{k}), \quad (3.6)$$

where

$$C_K(\mathbf{k}) = -(\mathbf{u}, \nabla E_P)_{\mathbf{k}}/2 - c^2(\mathbf{J}, \nabla h)_{\mathbf{k}}/2, \quad (3.7)$$

$$C_P(\mathbf{k}) = c^2(h, hd)_{\mathbf{k}}/2, \quad (3.8)$$

$$T_P(\mathbf{k}) = -c^2(h, \mathbf{u} \cdot \nabla h + hd/2)_{\mathbf{k}} \quad (3.9)$$

and

$$T_K(\mathbf{k}) = -(\mathbf{u}, \mathbf{u} \cdot \nabla \mathbf{J})_{\mathbf{k}}/2 - (\mathbf{J}, \mathbf{u} \cdot \nabla \mathbf{u})_{\mathbf{k}}/2 - (\mathbf{u}, d\mathbf{J})_{\mathbf{k}}/2. \quad (3.10)$$

The mean conversion from potential energy to kinetic energy can be computed from the two conversion spectral functions as $C = \sum_{\mathbf{k}} C_K(\mathbf{k}) = \sum_{\mathbf{k}} C_P(\mathbf{k})$.

3.1.2. Exact Kolmogorov law for irrotational flows

As in incompressible homogeneous isotropic turbulence, an exact Kolmogorov law for irrotational flows can be derived. It is convenient to start from the following form of the governing equations

$$\partial_t \mathbf{u} = -\nabla \cdot (|\mathbf{u}|^2/2) - c^2 \nabla h - \zeta_a \mathbf{e}_z \wedge \mathbf{u}, \quad (3.11)$$

$$\partial_t \mathbf{J} = -\partial_j (u_j \mathbf{J}) - \nabla E_p, \quad (3.12)$$

$$\partial_t h = -\nabla \cdot \mathbf{J}. \quad (3.13)$$

Assuming that the flow is irrotational and that there is no global rotation ($\zeta_a = 0$), it can be shown that

$$\partial_t (J'_i u_i) = -\partial_i (J'_i |\mathbf{u}|^2/2) - \partial'_i (u_j J'_j u'_i) - \partial_i (J'_i c^2 h) - \partial'_i (u_i E'_p) \quad (3.14)$$

and

$$\partial_t (h' h) = -\partial_i (h' J_i) - \partial'_i (h J'_i), \quad (3.15)$$

which gives

$$\begin{aligned} \partial_t (\mathbf{J}' \cdot \mathbf{u} + \mathbf{J} \cdot \mathbf{u}' + 2c^2 h' h) &= -\partial_i (J'_i |\mathbf{u}|^2/2) - \partial'_i (J_i |\mathbf{u}'|^2/2) - \partial'_i (u_j J'_j u'_i) - \partial_i (u'_j J_j u_i) \\ &\quad - c^2 \partial_i (J'_i h) - c^2 \partial'_i (J_i h') - \partial'_i (u_i E'_p) - \partial_i (u'_i E_p) \\ &\quad - 2c^2 \partial'_i (J'_i h) - 2c^2 \partial_i (J_i h'). \end{aligned} \quad (3.16)$$

We then assume homogeneity and take the ensemble average denoted by $\langle \cdot \rangle$. The separation vector is noted $\mathbf{r} = \mathbf{x}' - \mathbf{x}$. For every function $g(\mathbf{x}, \mathbf{x}')$, we have $\partial'_i \langle g \rangle = -\partial_i \langle g \rangle = \nabla_{\mathbf{r}} \langle g \rangle|_i$. We obtain

$$\begin{aligned} \partial_t (\mathbf{J}' \cdot \mathbf{u} + \mathbf{J} \cdot \mathbf{u}' + 2c^2 h' h) &= +\nabla_{\mathbf{r}} \cdot \langle \mathbf{J}' |\mathbf{u}|^2/2 - \mathbf{J} |\mathbf{u}'|^2/2 \rangle \\ &\quad - \nabla_{\mathbf{r}} \cdot \langle u_j J'_j \mathbf{u}' - u'_j J_j \mathbf{u} \rangle \\ &\quad - \nabla_{\mathbf{r}} \cdot \langle \mathbf{u} E'_p - \mathbf{u}' E_p \rangle \\ &\quad - c^2 \nabla_{\mathbf{r}} \cdot \langle \mathbf{J}' h - \mathbf{J} h' \rangle \end{aligned} \quad (3.17)$$

We then introduce the structure functions and the operator δ returning the increment of a variable between two points separated by \mathbf{r} , for example $\delta h(\mathbf{x}, \mathbf{r}) = h(\mathbf{x} + \mathbf{r}) - h(\mathbf{x})$. Using again homogeneity, we get

$$\langle (\delta h)^2 \delta \mathbf{u} \rangle = -\langle h'^2 \mathbf{u} \rangle + \langle h^2 \mathbf{u}' \rangle + 2\langle h h' \mathbf{u} \rangle - 2\langle h h' \mathbf{u}' \rangle \quad (3.18)$$

and

$$\langle |\delta \mathbf{u}|^2 \delta \mathbf{J} \rangle = \langle |\mathbf{u}|^2 \mathbf{J}' \rangle - \langle |\mathbf{u}'|^2 \mathbf{J} \rangle + \langle u_j u'_j \mathbf{J}' \rangle - \langle u_j u'_j \mathbf{J} \rangle, \quad (3.19)$$

which gives

$$2\partial_t (\mathbf{J}' \cdot \mathbf{u} + \mathbf{J} \cdot \mathbf{u}' + 2c^2 h' h) = \nabla_{\mathbf{r}} \cdot (\langle |\delta \mathbf{u}|^2 \delta \mathbf{J} \rangle + c^2 \langle (\delta h)^2 \delta \mathbf{u} \rangle). \quad (3.20)$$

Using isotropy and integrating yield an exact Kolmogorov law for one-layer shallow water irrotational turbulence

$$\langle |\delta \mathbf{u}|^2 \delta J_L \rangle + c^2 \langle (\delta h)^2 \delta u_L \rangle = -4\varepsilon r, \quad (3.21)$$

where ε is the energy dissipation rate and $J_L \equiv \mathbf{J} \cdot \mathbf{r}/|\mathbf{r}|$ and $u_L \equiv \mathbf{u} \cdot \mathbf{r}/|\mathbf{r}|$ are longitudinal increments.

3.2. Simple model for structure functions determined by a random set of shocks

Bouchaud *et al.* (1995) and Kuznetsov (2004) showed that the presence of discontinuities can strongly influence the statistics and in particular lead to very strong intermittency. We now present an extremely simple model based on the assumption that shocks totally dominate the flow. The structure functions are calculated by averaging increments over the total surface of the domain \mathcal{A} . Considering that the increments are produced only by discontinuity lines, we get

$$\begin{aligned}\langle |\delta h|^p \rangle &= \frac{1}{\mathcal{A}} \int_{\mathcal{A}} d^2 \mathbf{x} |\delta h(\mathbf{x})|^p \\ &\simeq \frac{r}{\mathcal{A}} \int_{\text{shocks}} ds |\sin \theta| |\Delta h(s)|^p,\end{aligned}\quad (3.22)$$

where θ is the angle between the shock line and the separation vector \mathbf{r} and $\Delta h(s)$ is the step in h at a shock. Assuming isotropy, the integral can be split and we get

$$\langle |\delta h|^p \rangle \simeq r \frac{L_s}{\mathcal{A}} \langle |\sin \theta| \rangle_{\theta} \langle |\Delta h(s)|^p \rangle_s = r \frac{L_s}{\mathcal{A}} \frac{2}{\pi} \langle |\Delta h(s)|^p \rangle_s, \quad (3.23)$$

where $\langle \cdot \rangle_{\theta}$ denotes the mean over θ , L_s is the total length of the shocks in the domain and $\langle \cdot \rangle_s$ denotes the mean over all shocks.

For velocity increments, we can also use a characteristic of the velocity singularities. The step in velocity is only in the component perpendicular to the shocks, which implies that the longitudinal and transverse increments are related by $\delta u_L = \delta u \sin \theta$, $\delta u_T = \delta u \cos \theta$. Applying the same averaging method, we obtain

$$\langle |\delta u_L|^p \rangle \simeq r \frac{L_s}{\mathcal{A}} \langle |\sin \theta|^{1+p} \rangle_{\theta} \langle |\Delta u(s)|^p \rangle_s \quad (3.24)$$

and

$$\langle |\delta u_T|^p \rangle \simeq r \frac{L_s}{\mathcal{A}} \langle |\sin \theta| |\cos \theta|^p \rangle_{\theta} \langle |\Delta u(s)|^p \rangle_s, \quad (3.25)$$

where $\Delta u(s)$ is the velocity step at a shock. These assumptions completely determine the ratio between the longitudinal and transverse structure functions, which can be analytically computed as

$$R_p(r) \equiv \frac{\langle |\delta u_L|^p \rangle}{\langle |\delta u_T|^p \rangle} = \frac{\langle |\sin \theta|^{1+p} \rangle_{\theta}}{\langle |\sin \theta| |\cos \theta|^p \rangle_{\theta}}, \quad (3.26)$$

giving the numerical values $R_2 = 2$, $R_3 = 6\pi/8$ and $R_4 = 8/3$.

Interestingly, for an isotropic and purely divergent flow ($\zeta = 0$), the longitudinal and transverse second order structure functions are exactly related by $\langle (\delta u_L)^2 \rangle = \partial_r(r \langle (\delta u_T)^2 \rangle)$ (Lindborg 2007). If we further assume than both second order structure functions follow the same scaling law $\langle (\delta u_L)^2 \rangle \propto \langle (\delta u_T)^2 \rangle \propto r^{\alpha}$, then we have $\langle (\delta u_L)^2 \rangle = (1+\alpha) \langle (\delta u_T)^2 \rangle$, which gives $R_2 = 2 \Leftrightarrow \alpha = 1$.

The shock model also provides predictions of the flatness factors of the velocity increments

$$F_L = \frac{\langle |\delta u_L|^4 \rangle}{\langle |\delta u_L|^2 \rangle^2} = r^{-1} \frac{\langle |\Delta u|^4 \rangle_s}{\langle |\Delta u|^2 \rangle_s^2} \frac{\langle |\sin \theta|^5 \rangle_{\theta}}{\langle |\sin \theta|^3 \rangle_{\theta}^2}, \quad (3.27)$$

$$F_T = \frac{\langle |\delta u_T|^4 \rangle}{\langle |\delta u_T|^2 \rangle^2} = r^{-1} \frac{\langle |\Delta u|^4 \rangle_s}{\langle |\Delta u|^2 \rangle_s^2} \frac{\langle |\sin \theta| |\cos \theta|^4 \rangle_{\theta}}{\langle |\sin \theta| |\cos \theta|^2 \rangle_{\theta}^2}, \quad (3.28)$$

and on the ratio of the two flatness factors, which is simply equal to $F_T/F_L = 1.5$ according to the model.

4. Numerical methods

4.1. Numerics

From a numerical point of view, it is convenient to solve for the eigenmodes of the linear operator \hat{q} and $\hat{a}_\pm = \hat{a}/2 \pm \omega_l \hat{d}/(2i)$. We thus consider the following modified governing equations

$$(\partial_t + f_{\text{diss}}(\mathbf{k}))\hat{q} = \hat{N}_q, \quad (4.1)$$

$$(\partial_t + f_{\text{diss}}(\mathbf{k}) \pm i\omega_l)\hat{a}_\pm = \hat{N}_\pm + \hat{f}_\pm, \quad (4.2)$$

where \hat{f}_\pm are forcing terms and \hat{N}_q and $\hat{N}_\pm = \hat{N}_a/2 \pm \omega_l \hat{N}_d/(2i)$ are non-linear terms computed from $\hat{\mathbf{N}}\mathbf{u} = -\zeta \mathbf{e}_z \wedge \mathbf{u} - \nabla |\mathbf{u}|^2/2$ and $\hat{N}_\eta = -\nabla \cdot (\eta \mathbf{u})$. We have removed the Newtonian viscous operator in (2.1) and added more general dissipative operators in (2.1) and (2.2). There is no strong physical motivations for this modification but, as discussed by Farge & Sadourny (1989), molecular dissipation of the form $\nu \nabla^2 \mathbf{u}$ is not necessarily a relevant model of the actual small-scale dissipation for shallow-water flows, which should rather be described as a transition from two-dimensional to three-dimensional motions before reaching the scales where dissipation actually occurs.

Equations (4.1-4.2) are simulated by means of a pseudo-spectral method with periodic boundary conditions. Time advancement is carried out by a classical fourth-order Runge-Kutta scheme for the nonlinear term and an exact integration for the linear and dissipative terms. This explicit integration is especially interesting at very high resolution and very large c when the shortest waves are very fast with frequency of the order of $\omega \simeq c \max(k)$. We use an adaptable time step method which maximizes the time step over a standard Courant-Friedrichs-Lowy condition (Lundbladh *et al.* 1999; Augier *et al.* 2012). Most of the aliasing is removed by truncating 8/9 of the modes along each direction (for a detail discussion on the issues of the non-conservation of the non-quadratic energy and the aliasing errors in the truncated one-layer shallow water model, see Farge & Sadourny 1989).

4.2. Forced dissipative statistically stationary simulations

We have carried out a number of simulations with large-scale forcing and small-scale dissipation for different resolutions and different values of the wave speed. The resolution is characterized by the number of nodes in the each direction, n , and has been varied from 240 to 7680. The wave speed c has been varied over two orders of magnitude from 10 to 1000. Table 1 presents the parameters for a set of representative simulations.

The ageostrophic variable a is forced in a shell in spectral space corresponding to relatively small wave numbers $5\delta k \leq |\mathbf{k}| \leq 8\delta k$, where $\delta k = 2\pi/L_h$. In the following, we use $L_h = 50$ in order to obtain a characteristic forcing wave number of order unity, $k_f \equiv 6\delta k \simeq 0.75$. The corresponding forcing scale is $L_f \equiv \pi/k_f \simeq 4.2$. Since only the ageostrophic variable is forced ($\hat{f}_d = 0$), (i) only the thickness fluctuation η is forced in the non-rotating case and (ii) the force terms in (4.2) are simply equal to $\hat{f}_\pm = \hat{f}_a/2$. In order to compute the force \hat{f}_a , we start from a pre-normalized force f_0 obtained from a normal random process decorrelated in time. The force is then normalized such that the quadratic part of the total energy $\langle |\mathbf{u}|^2 + c^2 \eta^2 \rangle/2$ is injected at a constant rate. The spectral injection rate of the quadratic energy averaged over one time step is (see

n	c	ν_8	ε	$\frac{k_{\max}}{k_{\text{diss}}}$	$\frac{k_{\text{diss}}}{k_f}$	F_f	$\min h$	$\frac{\max \mathbf{u} }{c}$
960	10	1.5e-10	1.03	2.46	29	0.111	0.25	0.96
1920	10	9.6e-13	1.00	2.46	58	0.110	0.37	0.92
3840	10	6.0e-15	1.01	2.46	116	0.110	0.39	1.01
7680	10	3.7e-17	1.03	2.46	231	0.111	0.32	0.95
960	20	1.5e-10	0.98	2.47	29	0.055	0.65	0.51
1920	20	9.6e-13	0.84	2.48	57	0.052	0.66	0.81
3840	20	6.0e-15	0.99	2.46	115	0.055	0.56	0.68
960	40	1.5e-10	0.99	2.46	29	0.027	0.81	0.24
1920	40	9.6e-13	1.01	2.46	58	0.028	0.78	0.28
3840	40	6.0e-15	0.98	2.47	115	0.027	0.77	0.29
7680	40	3.7e-17	0.94	2.47	230	0.027	0.76	0.32
960	100	1.5e-10	0.99	2.46	29	0.011	0.89	0.09
1920	100	9.6e-13	0.98	2.47	58	0.011	0.90	0.11
3840	100	6.0e-15	0.97	2.47	115	0.011	0.87	0.13
960	200	1.5e-10	0.99	2.46	29	0.005	0.95	0.05
1920	200	9.6e-13	0.99	2.46	58	0.005	0.94	0.06
3840	200	6.0e-15	0.90	2.47	115	0.005	0.94	0.06
960	400	1.5e-10	0.97	2.47	29	0.003	0.97	0.03
1920	400	9.6e-13	0.99	2.46	58	0.003	0.96	0.03
960	1000	1.5e-10	1.16	2.45	29	0.001	0.98	0.01
1920	1000	9.6e-13	0.91	2.47	57	0.001	0.98	0.01

TABLE 1. Overview of parameters for a set of representative simulations. The number of nodes in the each direction is denoted by n . The size of the numerical domain is equal to $L_h = 50$. Only the wave numbers $5\delta k \leq |\mathbf{k}| \leq 8\delta k$ are forced and the forcing wave number is defined as $k_f \equiv 6\delta k$ corresponding to a characteristic forcing scale of approximately $L_f \equiv \pi/k_f = 3.57$. $F_f = \varepsilon^{1/3}/(k_f^{1/3}c)$ is the forcing Froude number and $\max |\mathbf{u}|/c$ is the spatial and temporal maximum of a local Froude number.

appendix A)

$$P_q(\mathbf{k}, t) = \Re\{\hat{\mathbf{u}}(\mathbf{k})^* \cdot \hat{\mathbf{f}}(\mathbf{k}) + c^2 \hat{\eta}(\mathbf{k})^* \hat{f}_\eta(\mathbf{k})\} + (|\hat{\mathbf{f}}|^2 + c^2 |\hat{f}_\eta|^2) \delta t / 2, \quad (4.3)$$

where \Re denotes the real part. Writing $\hat{f}_a = \alpha \hat{f}_0$, it is straightforward to solve a second-order equation for the coefficient α in order to fix the injection rate $P_0 \equiv \sum_{\mathbf{k}} P_q(\mathbf{k}, t)$ to unity.

The energy is dissipated at the smallest resolved scales by a hyper-viscous operator, corresponding to a dissipative frequency equal to $f_{\text{diss}}(\mathbf{k}) = \nu_n |\mathbf{k}|^n$, with $n = 8$. The value of the hyperviscosity ν_8 is chosen such as the hyper-Kolmogorov wave number

$$k_{Kn} = \left(\frac{\nu_n^3}{\varepsilon} \right)^{\frac{1}{3n-2}}, \quad (4.4)$$

is well resolved, $k_{\text{diss}} = k_{Kn} \simeq k_{\max}/2.5$, where $k_{\max} = (8/9)\pi n/L_h$ is the maximum resolved wave number.

We have observed that when only the waves are forced, the vorticity does not increase and that when the vorticity is small enough, it does not significantly influence the waves. Therefore, we have chosen not to simulate a negligible vorticity field and to only solve equations (4.2) with $\zeta = 0$.

The time evolution of the instantaneous total energy is shown in figure 1 for differ-

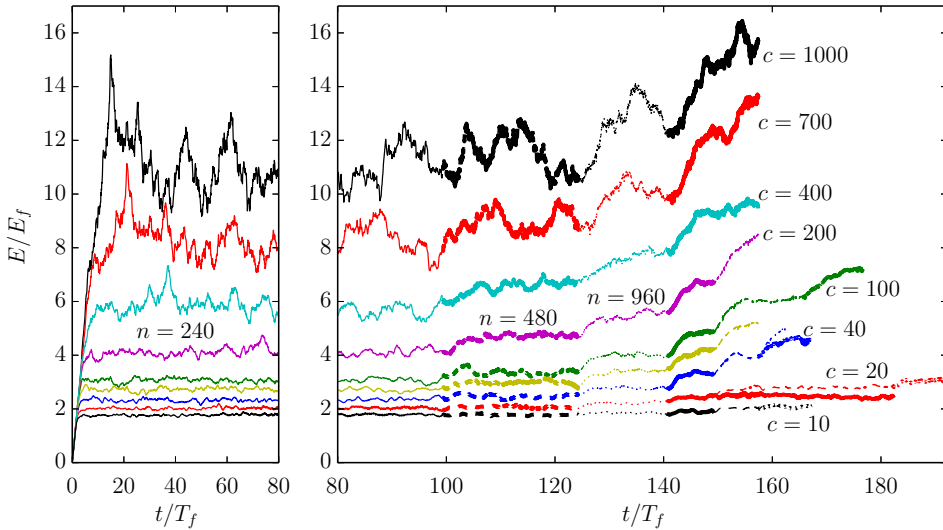


FIGURE 1. Space averaged energy $\langle h|\mathbf{u}|^2 + c^2 h^2 \rangle / 2$ versus time for different wave speeds c and resolutions n . The energy and the time are normalized by $E_f \equiv (P_0/k_f)^{2/3}$ and $T_f \equiv (P_0 k_f^2)^{-1/3}$, with $P_0 = 1 \simeq \varepsilon$. The colors corresponds to different wave speeds as indicated in the figure $c = 10, 20, 40, 70, 100, 200, 400, 700$ and 1000 . The different resolutions are represented by different types of lines: thin continuous lines, $n = 240$; thick dashed lines, $n = 480$; thin dotted lines, $n = 960$; thick continuous lines, $n = 1920$; thin dashed lines, $n = 3840$; thick dotted lines, $n = 5760$ and thin dotted dashed lines, $n = 7680$.

ent wave speeds c . The resolution and the dissipation wave number are progressively increased: $n = 240$ ($0 \leq t/T_f \leq 100$), $n = 480$ ($100 \leq t/T_f \leq 125$), $n = 960$ ($125 \leq t/T_f \leq 140$), $n = 1920$, $n = 3840$, $n = 5760$ and $n = 7680$, where $T_f \equiv (P_0 k_f^2)^{-1/3}$ is the characteristic forcing time. Each time the resolution is increased, the energy first sharply increases and then fluctuates. For most of the simulations, it is clear that a statistically stationary regime is reached. However, in the relatively short simulations at the highest resolution for the largest wave speeds ($n = 1920$, $c = 700$ and 1000), for some relatively short simulations with very large wave speed and/or very large resolution, there are large fluctuations and it is not absolutely certain whether a statistically stationary regime is reached. This is in particular the case for the simulations for $c = 700$, $n = 1920$ (thick red continuous line), $c = 200$, $n = 3840$ (thin magenta dashed line) and $c = 40$, $n = 7680$ (thin blue dotted dashed line). Note that these simulations are already quite numerically costly. For example, the simulation for $c = 1000$ and $n = 1920$ during slightly less than $20T_f$ corresponds to approximately 8×10^5 time steps.

Since the energy is injected at large scales and dissipated only at the smallest resolved scales, the existence of a statistically stationary regime implies a downscale flux of energy, which is equal to the large-scale energy injection rate. For the same energy injection rate and resolution, the mean energy increases with the wave speed, implying that when c increases the mean energy has to be larger to lead to the same downscale energy flux. The results presented in the following are from the statistically stationary regime. Apart from the snapshots, all shown quantities are averaged over a period corresponding to this regime.

Table 1 presents numerical and physical quantities for a set of representative simula-

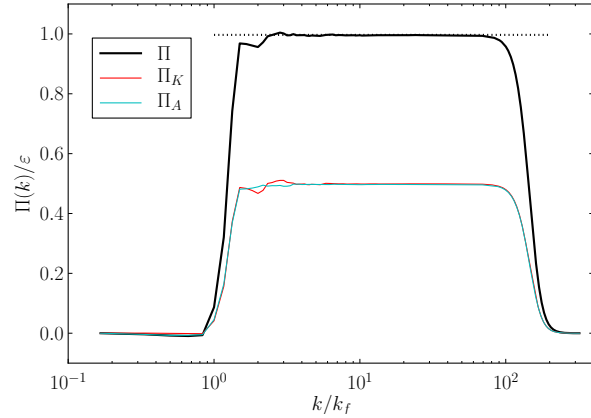


FIGURE 2. Spectral energy fluxes averaged over a long simulation for $c = 100$ and $n = 3840$. The fluxes are nondimensionalized by ε and plotted versus k/k_f .

tions. We characterize the simulations by the forcing Froude number

$$F_f \equiv \frac{\varepsilon^{1/3}}{k_f^{1/3} c}. \quad (4.5)$$

Since the characteristic forcing wave number and the dissipation rate are approximately equal to $k_f \equiv 6\delta k \simeq 0.75$ and $\varepsilon \simeq P_0 = 1$, the forcing Froude number is approximately inversely proportional to the wave speed: $F_f \simeq 1.1/c$. This allows us to simply use the wave speed to denote the simulations. The ratio k_{diss}/k_f gives an order of magnitude of the width of the inertial range. It is a physical quantity related to the numerical resolution on which the flow can depend. Table 1 also displays the minimum thickness $\min(h)$ characterizing the importance of the non-quadraticity of the energy, and $\max(|\mathbf{u}|/c)$, which can be interpreted as the maximum of a local Froude number.

5. Wave cascade without global rotation

5.1. Downscale energy cascade of waves

The spectral energy fluxes of total energy, KE and APE are plotted in figure 2 as functions of k/k_f . The fluxes are approximately zero at the wave numbers smaller than the forced wave numbers. They increase sharply at the forced wave numbers to values close to ε for the total energy flux and to 0.5ε for the KE and APE fluxes. The fluxes then decrease to zero over the dissipation range. The energy is transferred from the forced wave numbers to the dissipation wave numbers with a constant flux equal to the mean forcing and dissipation rates. There is an inertial range where the flux is constant and equipartitioned between equal KE and APE fluxes. However, at wave numbers $k \simeq 2k_f$, the flux is not exactly equal to ε . This is very likely related to the energy injection at wave numbers for which the force is zero, which is due to the non-quadraticity of the kinetic energy (see appendix A). Nevertheless this effect is non-negligible only for wave number of the order of $k \simeq 2k_f$, i.e. at the first harmonics of the forced wave numbers, such that there is a clear and wide inertial range between $k \gtrsim 3k_f$ to the dissipation range starting at wave number of the order of $k \sim 70k_f$.

Figure 3 shows the quantity $\langle \delta J_L | \delta \mathbf{u} |^2 \rangle + c^2 \langle \delta u_L (\delta h)^2 \rangle$ (black thick line) normalized by $4\varepsilon r$ for $c = 20$ and $n = 1920$. In this section, the brackets $\langle \rangle$ denote the average over space and time. The dotted straight line shows the quantity $4\varepsilon_q r$, where ε_q is the

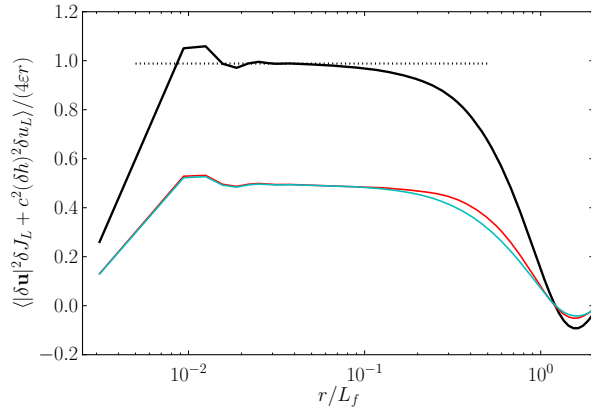


FIGURE 3. Third order structure functions involved in the exact Kolmogorov law (3.21) averaged over a long simulation for $c = 20$ and $n = 3840$. The structure functions are normalized by $4\epsilon_r$. Black thick line, $\langle \delta J_L |\delta \mathbf{u}|^2 \rangle + c^2 \langle \delta u_L (\delta h)^2 \rangle$; light thin line, $c^2 \langle \delta u_L (\delta h)^2 \rangle$; dark thin line, $\langle \delta J_L |\delta \mathbf{u}|^2 \rangle$. The dotted straight line shows $4\epsilon_q r$, where ϵ_q is the quadratic energy dissipation rate.

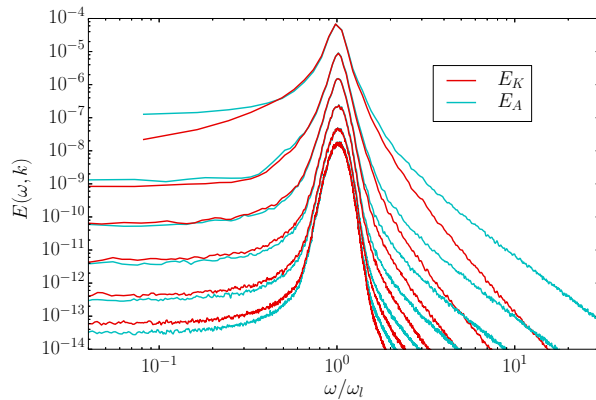


FIGURE 4. Spatio-temporal spectra of KE (dark lines) and APE (light lines) for $c = 20$ and $n = 3840$ versus ω/ω_l , where $\omega_l = ck$. From the larger to the smaller spectra, $k/\delta k = 12, 27, 62, 143, 327$, and 746 .

quadratic energy dissipation rate (see appendix A) which takes place at small scales. We see that the Kolmogorov law (3.21) is well satisfied between $r \simeq 0.02L_f$ and $r \simeq 0.1L_f$. The dark and light thin continuous lines correspond to the quantities $\langle \delta J_L |\delta \mathbf{u}|^2 \rangle$ and $c^2 \langle \delta u_L (\delta h)^2 \rangle$, respectively. These two quantities are nearly equal over the inertial and dissipation ranges, which is consistent with a wave cascade when $f = 0$. The agreement with the Kolmogorov law and the equality between $\langle \delta J_L |\delta \mathbf{u}|^2 \rangle$ and $c^2 \langle \delta u_L (\delta h)^2 \rangle$ are the equivalents in the separation space of the plateau in the total energy flux and the equality between Π_K and Π_A , respectively.

Figure 4 presents the spatio-temporal spectra plotted as a function of the normalized frequency ω/ω_l . In order to calculate these spectra, we have saved well-resolved time series of $\hat{d}(\mathbf{k})$ and $\hat{a}(\mathbf{k})$ for wave numbers inside particular shells such as $k \leq \mathbf{k} < k + \delta k$, computed the temporal spectrum of each signal and averaged over the wave numbers inside each shell. The spectra are strongly dominated by large peaks at $\omega = \omega_l$ indicating that the characteristic frequency for each wave number is the linear frequency. However, the widening of the peaks can be explained only by nonlinear effects. [The equipartition](#)

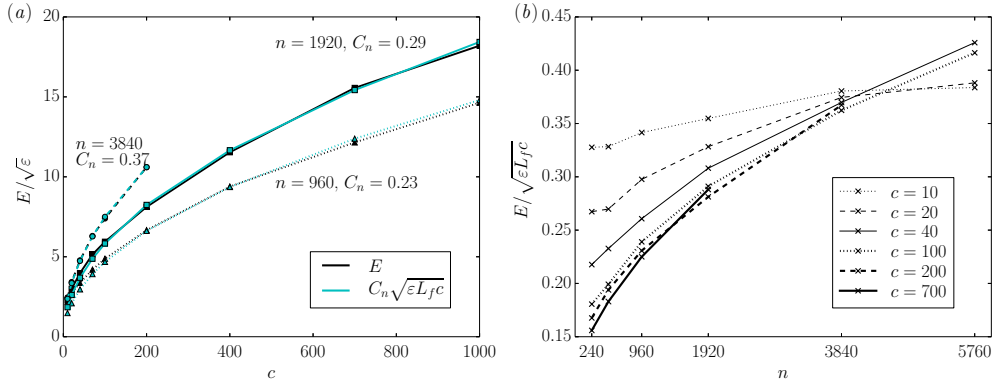


FIGURE 5. Time- and space-averaged energy $\langle h|\mathbf{u}|^2 + c^2 h^2 \rangle / 2$ of the statistically stationary flows. In (a), the energy is divided by $\sqrt{\varepsilon}$ and plotted versus c for 3 resolutions: $n = 960$, dotted lines; $n = 1920$, continuous lines and $n = 3840$, dashed lines. The cyan curves show the law $C_n \sqrt{\varepsilon L_f c}$, with C_n a fit coefficient. In (b), the energy is divided by $\sqrt{\varepsilon L_f c}$ and plotted versus n for six values of c as indicated in the legend.

between kinetic and potential energies is expected since the flow only consists of gravity waves and the total energy is nearly equal to the quadratic energy which is equal to the sum over all waves of their equipartitioned quadratic energy.

5.2. Time- and space-averaged energy as a function of c

Figure 5(a) shows the time- and space-averaged energy for the statistically stationary flows divided by the square root of the mean energy dissipation rate as a function of c and for three resolutions: $n = 960$, dotted lines; $n = 1920$, continuous lines and $n = 3840$, dashed lines. For all resolutions, the energy increases with c . More precisely, the curves can be well fitted to a law $E = C_n \sqrt{\varepsilon L_f c}$ (blue lines). However, the coefficient C_n varies with the resolution, i.e. with the effective Reynolds number. This is very different from the case of isotropic turbulence where the energy scales as $E \sim (\varepsilon L_f)^{2/3}$ and does not vary with the Reynolds number in the limit of very large Reynolds number. Weak wave turbulence theory predicts an energy-flux law of the form $E \propto \varepsilon^{1/(N-1)}$, where N is the number of waves involved in the nonlinear interactions (Nazarenko 2011). Therefore, the scaling $E = C_n \sqrt{\varepsilon L_f c}$ would correspond to interactions involving three waves. However, the hypothesis needed for applying the weak wave turbulence formulation are not fulfilled.

This effect of the increase of the energy with the resolution is investigated in figure 5(b) where the quantity $C_n = E/\sqrt{\varepsilon L_f c}$ is plotted as a function of the resolution. For $c = 10$ (dotted line), the waves are not very fast and the variation with the resolution is weak. However, in the limit of very fast waves ($c > 100$), the curves for the different wave speeds nearly collapse and increase at least up to $n = 5760$. The increase tends to saturate but it is difficult to know from our results what is the scaling of C_n as a function of the resolution and if it really saturates for very large n and c . In order to decide on this issue, we would need to run simulations in the very-fast-wave regime, $c > 100$, and at very large resolutions $n > 5760$. In this regime the energy fluctuations are large so that the simulations would have to be carried out for very long time in order to get a good convergence for the mean energy. Since the time step has to be extremely small in this regime, such simulations would be too costly.

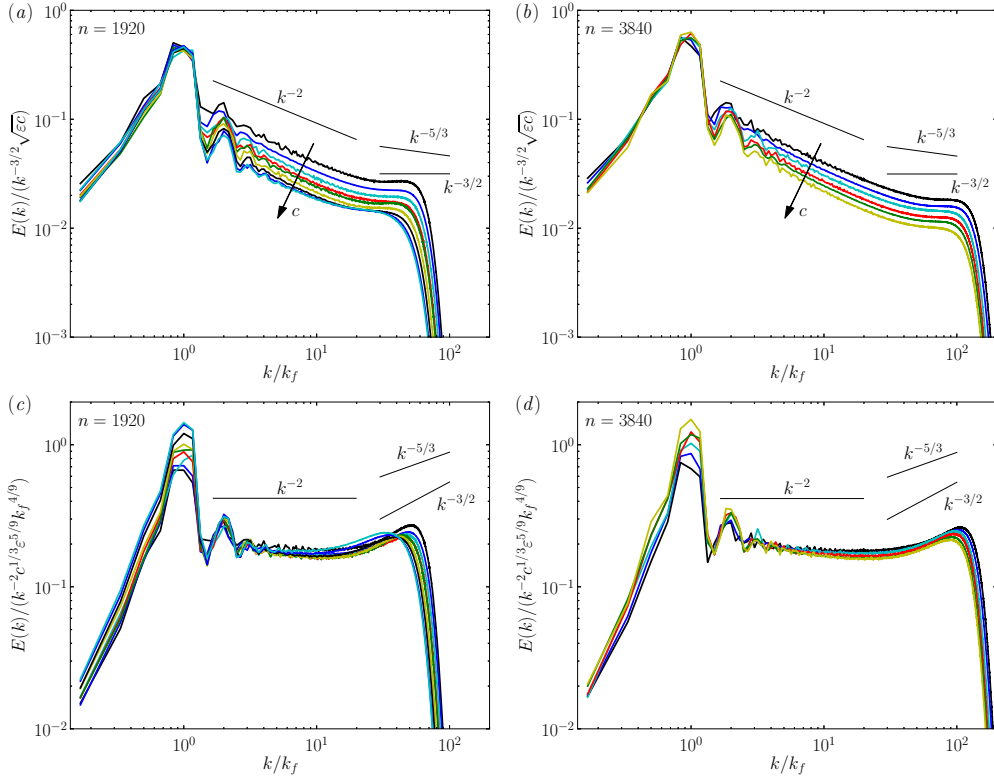


FIGURE 6. Compensated energy spectra versus k/k_f for different wave speeds c . The spectra are compensated by $k^{-3/2}\sqrt{\varepsilon c}$ in (a,b) and by $k^{-2}c^{1/3}\varepsilon^{5/9}k_f^{4/9}$ in (c,d). The resolution is $n = 1920$ in (a,c) and $n = 3840$ in (b,d). In (a,c), the wave speed goes from 10 to 1000 and in (b,d) from 10 to 200 (for the precise values, see figure 1).

5.3. Energy spectra

We now turn to the study of the energy spectra. A dimensional analysis based on the assumption that the spectra only depend on ε , c and k_f gives the following general expression

$$E_{\alpha,\beta}(k) = k^{-\alpha}\varepsilon^{\beta}c^{2-3\beta}k_f^{\alpha-1-\beta}, \quad (5.1)$$

where α and β are two free parameters.

The scaling of the energy as $\sqrt{\varepsilon L_f c}$ suggests that the spectra should scale like the Zakharov-Sagdeev spectrum, $E(k) \sim k^{-3/2}\sqrt{\varepsilon c}$, which is the prediction of weak wave turbulence theory for three-dimensional acoustic turbulence (Nazarenko 2011). The compensated spectra $E(k)/(k^{-3/2}\sqrt{\varepsilon c})$ are plotted in figure 6(a) for $n = 1920$ and in figure 6(b) for $n = 3840$. The different curves correspond to different wave speeds, going from $c = 10$ to $c = 1000$ for $n = 1920$ and from $c = 10$ to $c = 200$ for $n = 3840$. For both resolutions, the compensated spectra collapse at the energy-dominating small wave numbers. However, these compensated spectra are not flat in the inertial range and do not collapse in the inertial and dissipation ranges, i.e. for $k \gtrsim 2k_f$. In the inertial range, they follow a clear k^{-2} scaling law and there is a bottleneck in the dissipation range where the slope is close to $-3/2$. Kuznetsov (2004) showed that k^{-2} spectra can be explained by singularities and this scaling has already been observed in two-dimensional acoustic turbulence (Falkovich & Meyer 1996).

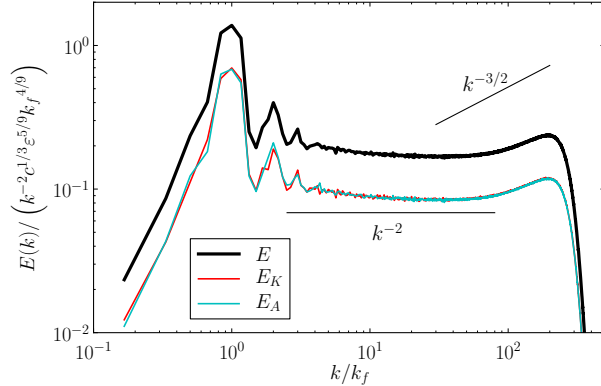


FIGURE 7. Compensated spectra of total energy (thick black line) kinetic energy (thin dark red line) and available potential energy (thin light blue line) for $c = 40$ and $n = 7680$.

Inserting $\alpha = 2$ in the spectrum (5.1) gives

$$E_\beta(k) = k^{-2} k_f^{1-\beta} c^{2-3\beta} \varepsilon^\beta \quad (5.2)$$

and we have found that the numerical spectra are very close to the spectrum $E_\beta(k)$ with $\beta = 5/9$. The compensated spectra $E(k)/(k^{-2}c^{1/3}\varepsilon^{5/9}k_f^{4/9})$ are plotted in figure 6(c) for $n = 1920$ and in figure 6(d) for $n = 3840$. The collapse is very good in the inertial range but we stress that we are not aware of any theory predicting the empirical spectrum $k^{-2}c^{1/3}\varepsilon^{5/9}k_f^{4/9}$.

Figure 7 shows the compensated spectra $E(k)/(k^{-2}c^{1/3}\varepsilon^{5/9}k_f^{4/9})$ of total energy (black line), KE (red line) and APE (blue line) for $c = 40$ and $n = 7680$. For all wave numbers, we have $E(k) = 2E_K(k) = 2E_A(k)$ since the flow only consists of [gravity](#) waves. The spectra are very close to k^{-2} in the inertial range over more than one decade and the shallowing to a slope close to $-3/2$ is clearly confined to the dissipation range. This confirms that this bump is due to a dissipation effect and that there is no wide $k^{-3/2}$ spectrum even at very large resolutions.

In subsection 5.1, we have shown that third-order structure functions scale like r since there is a downscale energy cascade. The Kolmogorov method predicts $k^{-5/3}$ -spectra but the numerical spectra are much steeper in the inertial range, with a slope equal to -2. The fact that third-order and second-order quantities can not be simply related by the Kolmogorov scaling implies that the cascade is very intermittent.

5.4. Effect of the shocks and intermittency

Figure 8 shows the normalized thickness h (figures 8a,b) and the y -component of the velocity u_y (figures 8c,d) for $c = 20$ (figures 8a,c) and $c = 200$ (figures 8b,d). These wave speeds correspond to a moderate forcing Froude number $F_f \sim 0.05$ and to a very small forcing Froude number $F_f \sim 0.005$, respectively. The normalized surface displacement $\eta = h - 1$ is of order 0.3 for $c = 20$ and one order of magnitude smaller, 0.03, for $c = 200$. The typical velocity is also much smaller than the wave speed, with $u_y/c \sim 0.2$ for $c = 20$ and $u_y/c \sim 0.03$ for $c = 200$. This confirms that the flows are in a fast-wave regime, especially for $c = 200$. However, many discontinuities can be seen in both fields h and u_y . These discontinuities are hydraulic jumps, which are the equivalent to shocks in a compressible flows. [Baines \(1998\)](#) provides a theoretical prediction for the velocity

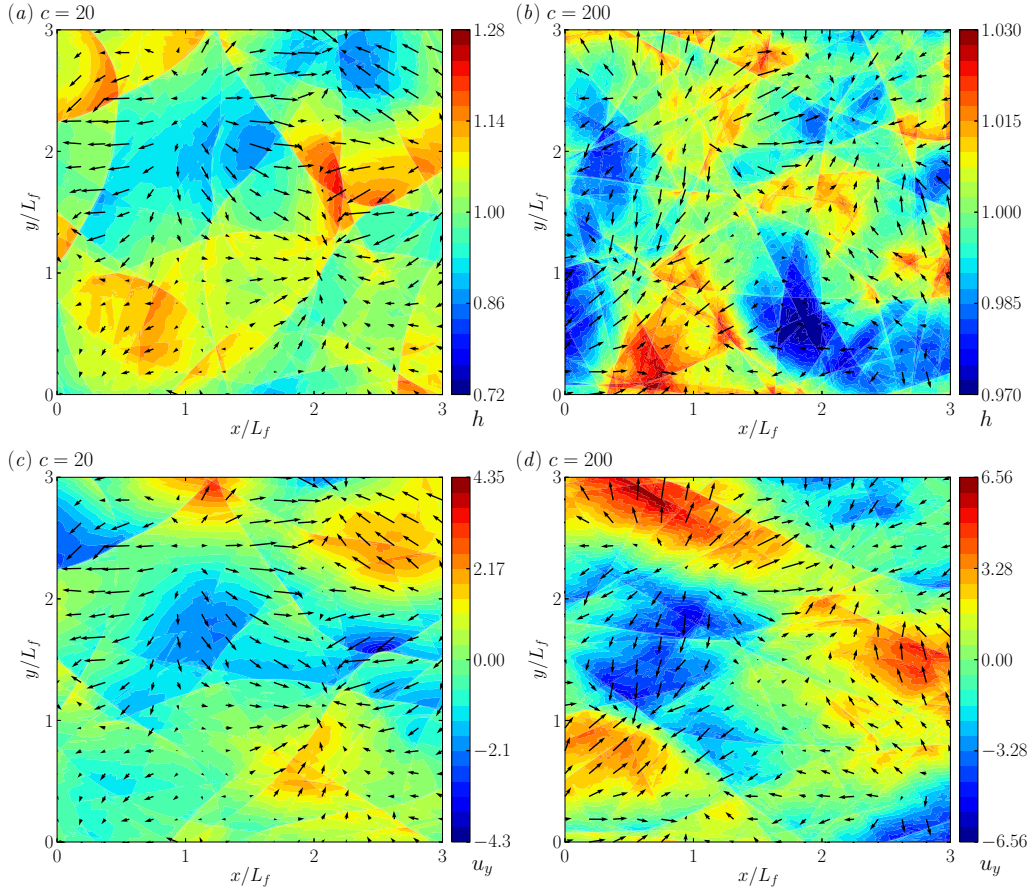


FIGURE 8. Snapshots for $n = 1920$ and two values of the wave speed $c = 20$ (a,c) and $c = 200$ (b,d). The colors represent the thickness in (a,b) and the y -component of the velocity in (c,d). The arrows represent the velocity field. The coordinates are nondimensionalized by the characteristic scale of the forcing $L_f = 3.57$.

of the hydraulic jumps is one-layer shallow-water flow:

$$c_s = c \sqrt{\frac{h_+}{h_-} \frac{h_+ + h_-}{2}}, \quad (5.3)$$

where h_+ and h_- are the dimensionless thickness before and after the jump. We have verified that the velocity of the discontinuities in the simulations is consistent with this theoretical prediction, implying that the associated Froude number (or Mach number) is of the order unity.

In between the shocks, the flow is very smooth for $c = 20$ and slightly more irregular for $c = 200$.

Figures 8(c,d) display the y -component of the velocity. There are less discontinuities in this quantity than in the thickness. More precisely, the h -discontinuity lines that are along the y -axis are not associated with corresponding discontinuities of the y -component of the velocity. This can be seen for example for the shock at $x/L_f \simeq 0.4$ and $y/L_f \simeq 2.1$ in figures 8(a) and 8(c). This illustrates that the singularity in the velocity is in the

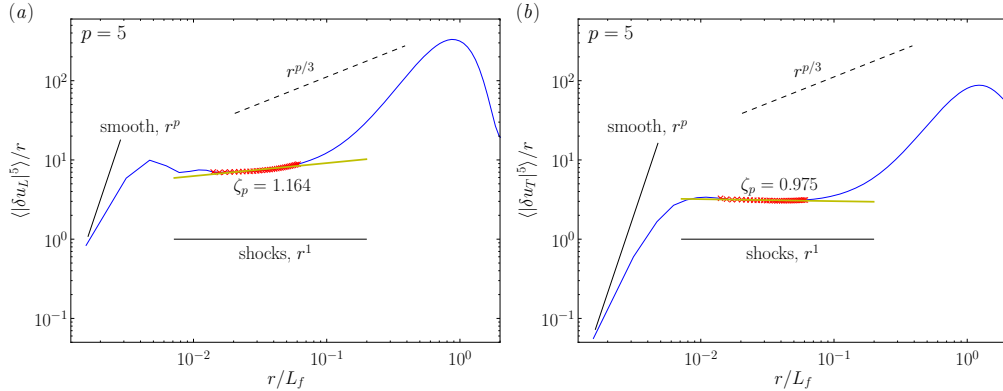


FIGURE 9. Compensated fifth-order structure functions $\langle |\delta u_L|^5 \rangle / r$ of (a) the longitudinal increments and (b) the transverse increments. The crosses indicate the range of separation r where the exponent ζ_p is computed. The dashed lines correspond to the Kolmogorov scaling laws $r^{p/3}$ and $\zeta_p = p/3$. The wave speed and the resolution are $c = 40$ and $n = 7680$.

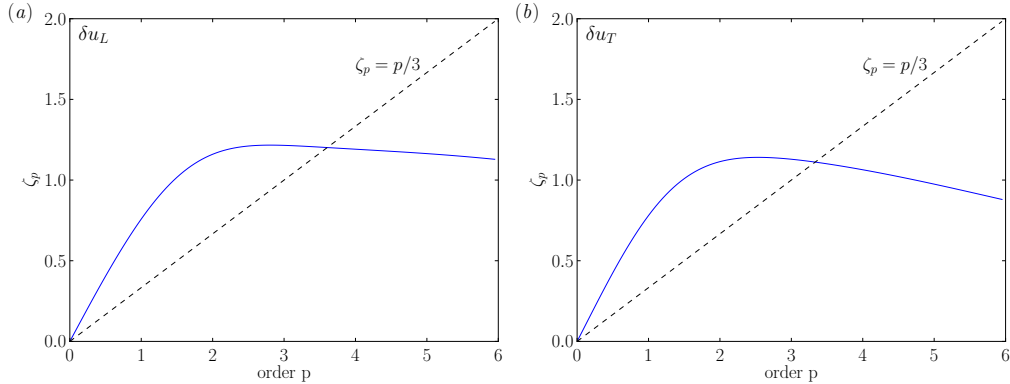


FIGURE 10. Exponents ζ_p of the structure functions of (a) the longitudinal increments and (b) the transverse increments versus the order p . The dashed lines correspond to the Kolmogorov scaling laws $r^{p/3}$ and $\zeta_p = p/3$. The wave speed and the resolution are $c = 40$ and $n = 7680$.

component perpendicular to the shock line, which is the assumption on the structure of the velocity discontinuities used in the model presented in § 3.2.

The shock model derived in subsection 3.2 predicts that structure functions of all orders should scale linearly with r . Figure 9 presents fifth-order structure functions compensated by r . Figures 9(a) and 9(b) correspond to the structure functions computed from the longitudinal increments and the transverse increments, respectively. The structure functions compensated by r are nearly flat between $r \simeq 0.012L_f$ and $r \simeq 0.06L_f$, showing that they scale like r on this relatively narrow range of scale compared to the inertial range. The r -scaling is very different from the slope of the fifth-order structure functions calculated from the Kolmogorov scaling $\zeta_5 = p/3 \simeq 1.66$ (dashed straight line). This shows that the wave cascade is strongly intermittent and that this intermittency can be explained by the presence of discontinuities related to the shocks.

The slope of the structure functions of order p over the range $0.012L_f \leq r \leq 0.06L_f$, ζ_p , are plotted in figure 10(a) for the longitudinal increments and in figure 10(b) for the transverse increments. The exponents are very far from the Kolmogorov scaling $\zeta_p = p/3$. They increase as p for $p \ll 1$, saturate to a value close to 1 for $p > 2$ and tend to decrease

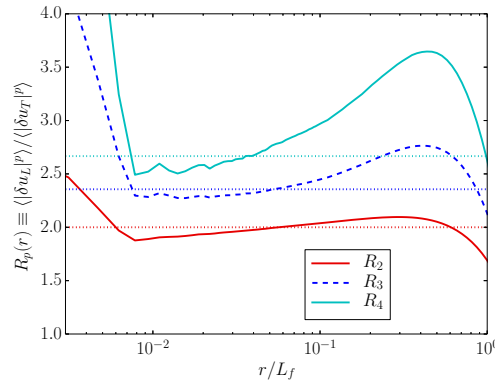


FIGURE 11. Ratio of the structure functions of the velocity increments $R_p(r) \equiv \langle |\delta u_L|^p \rangle / \langle |\delta u_T|^p \rangle$ for $p = 2, 3$ and 4 . The dotted straight lines indicate the values computed by the shock model: $R_2 = 2$, $R_3 = 6\pi/8$ and $R_4 = 8/3$. The wave speed and the resolution are $c = 10$ and $n = 7680$.

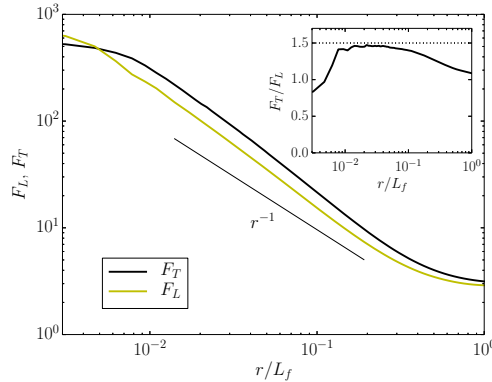


FIGURE 12. Flatness of the longitudinal and transverse increments for $c = 10$ and $n = 7680$. The straight continuous lines indicate the r^{-1} -scaling and the straight dashed line the $r^{-3/2}$ -scaling. The inset shows the ratio F_T/F_L and the corresponding value computed by the shock model, $F_T/F_L = 1.5$.

for $p > 3$. A similar shape of the ζ_p function has been predicted for Burger turbulence (Bouchaud *et al.* 1995). The shape of ζ_p at very small p is determined by the scaling of the smallest velocity increments and the p^1 -variation shows that these smallest increments scale like $\delta u \sim r^p$. The plateau at $p > 2$ is a consequence of the dominance by shocks of the largest increments. Note that these results are obtained for a relatively small forcing Froude number $F_f \simeq 0.03$ corresponding to $c = 40$. The function ζ_p has approximately the same extreme shape for a larger Froude number $F_f \simeq 0.01$, corresponding to $c = 10$. Note also that the decrease of ζ_p for $p > 3$ is anomalous, which could be due to the relatively narrow width of the range over which ζ_p is computed.

The functions $R_p = \langle |\delta u_L|^p \rangle / \langle |\delta u_T|^p \rangle$ are plotted in figure 11 for $p = 2$ to 4 . The predictions of the shock model, $R_2 = 2$, $R_3 = 6\pi/8$ and $R_4 = 8/3$, are also plotted in dotted lines for comparison. We see that the numerical results are reasonably close to these predictions. However, the agreement is less good for smaller Froude number (not shown). The structure functions are fully determined by shocks only for Froude numbers that are not too small, which is consistent with the snapshots in figure 8 showing that the fields between the shocks are more irregular for the smallest Froude number.

n	c	ν_8	f	Ro	Bu	ε	k_{\max}/k_{diss}	k_{diss}/k_f	F_f	$\min h$	$\frac{\max \mathbf{u} }{c}$
1920	20	9.6e-13	0	∞	∞	0.99	2.46	58	0.055	0.59	0.56
1920	20	9.6e-13	7.5	0.11	4	0.96	2.47	58	0.054	0.67	0.52
1920	20	9.6e-13	10.7	0.076	2	0.93	2.47	58	0.054	0.70	0.62
1920	20	9.6e-13	15.1	0.052	1	0.85	2.48	57	0.052	0.70	0.65
1920	20	9.6e-13	21.3	0.037	0.5	0.84	2.48	57	0.052	0.66	0.81

TABLE 2. Overview of parameters for the simulations used to study the effect of rotation.

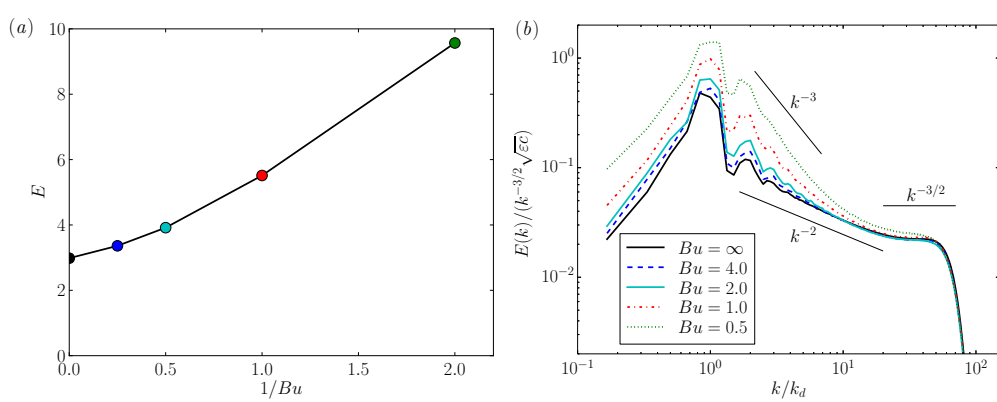
FIGURE 13. Effect of the rotation: (a) mean energy versus k_d/k_f and (b) energy spectra for $c = 20$ and $n = 1920$.

Figure 12 shows the flatness of the longitudinal and transverse increments, computed from a numerical simulation for $c = 10$ and $n = 7680$. For a Gaussian probability distribution the flatness factor is equal to 3 whereas the shock model predict flatness factors scaling like r^{-1} . We see that here the flatness factors are much larger than 3, of the order of 10^3 . Remarkably, they scale approximately as r^{-1} as predicted by the shock model and the ratio F_T/F_L is very close to the predicted value 1.5.

6. Effects of global rotation

In order to study the effects of system rotation, we have carried out four supplementary simulations for $c = 20$, $n = 1920$ and constant and non-zero Coriolis parameter f . The values of f have been chosen such that to yield relatively small Rossby numbers

$$Ro_f = \frac{\varepsilon^{1/3} k_f^{2/3}}{f} \lesssim 0.1, \quad (6.1)$$

and to span a range of Burger number,

$$Bu = \left(\frac{k_f}{k_d} \right)^2 = \left(\frac{Ro_f}{F_f} \right)^2, \quad (6.2)$$

going from 0.5 to 4. For these moderate values of global rotation, a statistically stationary regime is also reached. Table 2 displays the parameters for these simulations.

Figure 13(a) shows the mean energy as a function of the Burger number. We see that for $Bu = 2$ and 4, the mean energy is very close to the value obtained for the non-rotating case. However, when $k_f < k_d$, i.e. for $Bu < 1$, the mean energy increases. Figure 13(b)

presents the spectra for the same simulations. The spectra for $Bu = 2$ and 4 are very close to the spectra for $f = 0$, which confirms that a weak rotation does not deeply modify the non-rotating results. We have also verified that for the moderate rotation rates corresponding to $Bu > 1$, the other results presented in section 5 on the non-rotating wave cascade are only weakly modified. In particular, the results for $Bu = \infty$ and $Bu = 4$ are very similar.

7. Conclusions

We have numerically investigated one-layer shallow-water flows forced with medium-scale waves and dissipated at small scales. First, we have focused on the non-rotating case and varied the resolution and the wave speed over a wide range. The spectral energy budget for the full non-quadratic energy has been derived and has allowed us to show that the KE and the APE fluxes are constant and equal over a wide range of wave numbers. The KE and APE spatio-temporal spectra present equal and very strong peaks at the linear wave frequency. These two results show that there is a downscale energy cascade of non-dispersive waves, explaining the generation of statistically stationary flows. We have derived an exact Kolmogorov law for the one-layer shallow-water flow based on the assumption that there is a constant energy flux due to a purely divergent flow and verified that the numerical results are in agreement with this theoretical law.

The time- and spaced-averaged energy scales like $E = C_n \sqrt{\varepsilon L_f c}$ and increases with the resolution at least up to $n = 5760$. The spectra scale like the Zakharov-Sagdeev spectrum $k^{-3/2} \sqrt{\varepsilon c}$ at relatively small wave numbers $k \lesssim 2k_f$ and like $k^{-2} c^{1/3} \varepsilon^{5/9} k_f^{4/9}$ over the inertial range. We stress that we lack any convincing theoretical explanations for these scaling laws and we hope our results will motivate theoretical investigations on these challenging issues.

Nevertheless, the k^{-2} scaling can be explained by the presence of discontinuities (Kuznetsov 2004). The snapshots indeed show very sharp hydraulic jumps, which are the equivalent of shocks in compressible flows. Following Bouchaud *et al.* (1995) and Weinan *et al.* (1997), we have built a simple model based on the assumption that the structure functions are determined only by shocks. Using only this hypothesis, we explain the extreme intermittent characteristics of the flows, i.e. the r^1 -scaling of the structure functions of order larger than 2 and the r^{-1} -scaling of the flatness. Adding a simple hypothesis on the structure of the velocity field across the shocks, namely $\delta u_L = \delta u \sin \theta$ and $\delta u_T = \delta u \cos \theta$, where θ is the angle between the shock line and the separation vector, we have predicted the values of ratios of structure functions $R_p(r) \equiv \langle |\delta u_L|^p \rangle / \langle |\delta u_T|^p \rangle$ and of the flatness factors $F_T/F_L = 1.5$. Finally, we have shown that as long as $k_f > k_d$, the dispersion added by the rotation does not prevent the production of the regime studied in the non-rotating case and only weakly modify the results on the wave cascade.

Our results on the dynamics of the wave energy cascade in the one-layer shallow-water model can yet give interesting informations on the interpretation of turbulent measurements in geophysical fluids. Since we have shown in this case that many statistical results are dominated by the effects of the discontinuities due to shocks, we can conjecture that the discontinuities or front in the atmosphere can significantly influence the cascade processes and the statistical results. It would be interesting in the future to quantify the effects of the processes of frontogenesis in terms of downscale energy cascade in geophysical flows.

Acknowledgements

The authors thank Gregory Falkovich and Sergey Nazarenko for valuable comments and suggestions regarding the interpretation of the simulations.

Appendix A. Kinetic energy dissipation and forcing rates

In this appendix, we give the expressions of the kinetic energy dissipation and forcing rates, which are unusual for the one-layer shallow-water model since the kinetic energy has not a quadratic expression.

We consider viscous operators such as $\partial_t \mathbf{u}|_{\text{diss}} = -\nu_n i^{-n} \nabla^n \mathbf{u}$ and $\partial_t \eta|_{\text{diss}} = -\nu_n i^{-n} \nabla^n \eta$, with n even. The values $n = -4, 0, 2$ and 8 correspond to hypo-viscosity, linear damping, newtonian viscosity and hyper-viscosity, respectively. In this study, we have only used the value $n = 8$. Note that the dissipation operator is applied on η and not on h . Using $\partial_t \mathbf{J}|_{\text{diss}} = h \partial_t \mathbf{u}|_{\text{diss}} + \mathbf{u} \partial_t h|_{\text{diss}} = -\nu_n i^{-n} (h \nabla^n \mathbf{u} + \mathbf{u} \nabla^n \eta)$, the KE dissipation rate can be computed as

$$\partial_t \langle E_K \rangle_{\mathbf{x}}|_{\text{diss}} = \langle \partial_t \mathbf{u}|_{\text{diss}} \cdot \mathbf{J} + \mathbf{u} \cdot \partial_t \mathbf{J}|_{\text{diss}} \rangle / 2, \quad (\text{A } 1)$$

$$= -\nu_n i^{-n} \langle \mathbf{J} \cdot \nabla^n \mathbf{u} + |\mathbf{u}|^2 \nabla^n \eta / 2 \rangle \quad (\text{A } 2)$$

$$= - \sum_{\mathbf{k}} 2f_{dn} E_K(\mathbf{k}) - \sum_{\mathbf{k}} f_{dn} (|\mathbf{u}|^2 / 2, \eta)_{\mathbf{k}}, \quad (\text{A } 3)$$

where $f_{dn}(\mathbf{k}) = \nu_n |\mathbf{k}|^n$ is the dissipative frequency. The first term of the rhs is the usual term but there is also an additional term that is not negatively defined.

The spectral injection rate of quadratic kinetic energy averaged over one time step is

$$P_K(\mathbf{k}, t) = \frac{1}{\delta t} \int_t^{t+\delta t} dt' (\mathbf{u}(t'), \mathbf{f})_{\mathbf{k}} = (\mathbf{u}, \mathbf{f})_{\mathbf{k}} + |\mathbf{f}|^2 \delta t / 2, \quad (\text{A } 4)$$

where we have used the fact that the forcing \mathbf{f} is constant over the time step. In order to calculate the total KE injection rate, we have to take into account the non-quadratic term in the expression of the kinetic energy. The forcing terms are $\partial_t \mathbf{u}|_f = \mathbf{f}$, $\partial_t h|_f = f_h$ and $\partial_t \mathbf{J}|_f = \mathbf{f}_{\mathbf{J}} = h \mathbf{f} + \mathbf{u} f_h$ so that the instantaneous injection rate can be written as

$$P_{K_{\text{inst}}}(\mathbf{k}, t) = \partial_t E_K(\mathbf{k}, t)|_f = (\mathbf{J}, \mathbf{f})_{\mathbf{k}} / 2 + (\mathbf{u}, \mathbf{f}_{\mathbf{J}})_{\mathbf{k}} / 2. \quad (\text{A } 5)$$

Averaging over one time step, we obtain

$$P_K(\mathbf{k}, t) = \frac{1}{\delta t} \int_t^q t + \delta t dt' P_{K_{\text{inst}}}(\mathbf{k}, t') \quad (\text{A } 6)$$

$$= \frac{1}{\delta t} \int_t^{t+\delta t} dt' [(\mathbf{J}(t'), \mathbf{f})_{\mathbf{k}} / 2 + (\mathbf{u}(t'), h(t') \mathbf{f} + \mathbf{u}(t') f_h)_{\mathbf{k}} / 2]. \quad (\text{A } 7)$$

Using the estimates $\mathbf{u}(t') = \mathbf{u}(t) + \mathbf{f}(t' - t)$, $h(t') = h(t) + f_h(t' - t)$ and $\mathbf{J}(t') = \mathbf{J}(t) + \mathbf{f} f_h(t' - t)^2$, the KE injection rate averaged over one time step can be computed at the leading order as

$$\begin{aligned} P_K(\mathbf{k}, t) \simeq & (\mathbf{J}, \mathbf{f})_{\mathbf{k}} / 2 + (\mathbf{u}, \mathbf{f}_{\mathbf{J}})_{\mathbf{k}} / 2 \\ & + [(\mathbf{f}, \mathbf{f}_{\mathbf{J}})_{\mathbf{k}} / 2 + (\mathbf{u}, f_h \mathbf{f})_{\mathbf{k}}] \delta t / 2. \end{aligned} \quad (\text{A } 8)$$

REFERENCES

- AUGIER, P., CHOMAZ, J.-M. & BILLANT, P. 2012 Spectral analysis of the transition to turbulence from a dipole in stratified fluids. *J. Fluid Mech.* **713**, 86–108.

- BAINES, P. G. 1998 *Topographic effects in stratified flows*. Cambridge University Press.
- BOUCHAUD, J. P., MEZARD, M. & PARISI, G. 1995 Scaling and intermittency in Burgers turbulence. *Phys. Rev. E* **52** (4, A), 3656–3674.
- CHARNEY, J. G. 1971 Geostrophic turbulence. *J. Atmos. Sci.* **28** (6), 1087–&.
- FALKOVICH, G. & MEYER, M. 1996 Two-dimensional acoustic turbulence. *Phys. Rev. E* **54**, 4431–4434.
- FALKOVICH, G. E. & MEDVEDEV, S. B. 1992 Kolmogorov-like spectrum for turbulence of inertial-gravity waves. *Europhys. Lett.* **19** (4), 279–284.
- FARGE, M. & SADOURNY, R. 1989 Wave vortex dynamics in rotating shallow-water. *J. Fluid Mech.* **206**, 433–462.
- FREHLICH, R. & SHARMAN, R. 2010 Climatology of Velocity and Temperature Turbulence Statistics Determined from Rawinsonde and ACARS/AMDAR Data. *J. Appl. Meteor. Climatol.* **49**, 1149–1169.
- HAMILTON, K., TAKAHASHI, Y. O. & OHFUCHI, W. 2008 Mesoscale spectrum of atmospheric motions investigated in a very fine resolution global general circulation model. *J. Geophys. Res.-Atmos.* **113**, D18110.
- KOSHYK, J. N. & HAMILTON, K. 2001 The Horizontal Kinetic Energy Spectrum and Spectral Budget Simulated by a High-Resolution Troposphere-Stratosphere-Mesosphere GCM. *J. Atmos. Sci.* **58** (4), 329–348.
- KRAICHNAN, R. H. 1967 Inertial ranges in two-dimensional turbulence. *Phys. Fluids* **10** (7), 1417–1423.
- KUZNETSOV, E. A. 2004 Turbulence spectra generated by singularities. *JETP Lett.* **80** (2), 83–89.
- LAHAYE, N. & ZEITLIN, V. 2012 Decaying vortex and wave turbulence in rotating shallow water model, as follows from high-resolution direct numerical simulations. *Phys. Fluids* **24** (11).
- LARICHEV, V. D. & MCWILLIAMS, J. C. 1991 Weakly decaying turbulence in an equivalent-barotropic fluid. *Phys. Fluids A - Fluid Dyn.* **3** (5, 1), 938–950.
- LINDBORG, E. 1999 Can the atmospheric kinetic energy spectrum be explained by two-dimensional turbulence? *J. Fluid Mech.* **388**, 259–288.
- LINDBORG, E. 2007 Horizontal wavenumber spectra of vertical vorticity and horizontal divergence in the upper troposphere and lower stratosphere. *J. Atmos. Sci.* **64** (3), 1017–1025.
- LORENZ, E. 1980 Attractor sets and quasi-geostrophic equilibrium. *J. Atmos. Sci.* **37** (8), 1685–1699.
- LUNDBLADH, A., BERLIN, S., SKOTE, M., HILDINGS, C., CHOI, J., KIM, J. & HENNINGSON, D. S. 1999 An efficient spectral method for simulation of incompressible flow over a flat plate. *Trita-mek. Tech. Rep.* **11**.
- MOHEBALHOJEH, A. R. & DRITSCHEL, D. G. 2000 On the representation of gravity waves in numerical models of the shallow-water equations. *Q. J. R. Meteorol. Soc.* **126** (563), 669–688.
- NASTROM, G. D. & GAGE, K. S. 1985 A climatology of atmospheric wavenumber spectra of wind and temperature observed by commercial aircraft. *J. Atmos. Sci.* **42** (9), 950–960.
- NAZARENKO, S. 2011 *Wave turbulence*, , vol. 825. Springer Verlag.
- POLVANI, L. M., MCWILLIAMS, J. C., SPALL, M. A. & FORD, R. 1994 The coherent structures of shallow-water turbulence: Deformation-radius effects, cyclone/anticyclone asymmetry and gravity-wave generation. *Chaos* **4** (2), 177–U16.
- SADOURNY, R. 1975 The dynamics of finite-difference models of the shallow-water equations. *J. Atmos. Sci.* **32** (4), 680–689.
- SKAMAROCK, W. C. 2004 Evaluating mesoscale NWP models using kinetic energy spectra. *Mon. Weather Rev.* **132** (12), 3019–3032.
- SPALL, M. A. & MCWILLIAMS, J. C. 1992 Rotational and gravitational influences on the degree of balance in the shallow-water equations. *Geophys. Astrophys. Fluid Dyn.* **64** (1-4), 1–29.
- VALLIS, G. K. 2006 *Atmospheric and Oceanic Fluid Dynamics*. Cambridge University Press.
- VANNESTE, J. 2013 Balance and spontaneous wave generation in geophysical flows. *Annu. Rev. Fluid Mech.* **45**, 147–172.
- WARN, T. 1986 Statistical mechanical equilibria of the shallow-water equations. *Tellus Ser. A-Dyn. Meteorol. Oceanol.* **38** (1), 1–11.

- WEINAN, E., KHANIN, K., MAZEL, A. & SINAI, Y. 1997 Probability distribution functions for the random forced burgers equation. *Phys. Rev. Lett.* **78** (10), 1904–1907.
- WIRTH, A. 2013 Inertia-gravity waves generated by near balanced flow in 2-layer shallow water turbulence on the β -plane. *Nonlin. Processes Geophys.* **20**, 25–34.
- YUAN, L. & HAMILTON, K. 1994 Equilibrium dynamics in a forced-dissipative f-plane shallow-water system. *J. Fluid Mech.* **280**, 369–394.
- ZAKHAROV, V. E., L'VOV, V. S. & FALKOVICH, G. 1992 *Kolmogorov spectra of turbulence 1. Wave turbulence.*, , vol. 1. Springer-Verlag.